

Designing Band Gaps with Randomly Distributed Sub-Wavelength Helmholtz Resonators

Paulo S. Piva¹, Art L. Gower¹, I. David Abrahams²

¹School of Mechanical, Aerospace and Civil Engineering, University of Sheffield, Mappin Street, Sheffield, England, S1 4DT Sheffield, United Kingdom

²Department of Applied Mathematics and Theoretical Physics, University of Cambridge, Wilberforce Road, Cambridge, England, CB3 0WA, United Kingdom

May 8, 2025

Abstract

It is well-known that band gaps, in the frequency domain, can be achieved by using periodic metamaterials. However it has been challenging to design materials with broad band gaps or that have multiple overlapping band gaps. For periodic materials this difficulty arises because many different length scales would have to be repeated periodically within the same structure to have multiple overlapping band gaps. Here we present an alternative: to design band gaps with disordered materials. We show how to tailor band gaps by choosing any combination of Helmholtz resonators that are positioned randomly within a host acoustic medium. One key result is that we are able to reach simple formulae for the effective material properties, which work over a broad frequency range, and can therefore be used to rapidly design tailored metamaterials. We show that these formulae are robust by comparing them with high-fidelity Monte Carlo simulations over randomly positioned resonant scatterers.

1 Introduction

Metamaterials are artificially fabricated composite materials which have properties not found in nature; they are designed for specific and targeted applications [1]. Wave motion control is an important application for electromagnetics, elastodynamics, and acoustics. There are many examples of fabricated materials that can distort or bend the path that waves propagate along, allow negative refraction [2], block specific frequencies [3], or cloak (i.e. render invisible) certain parts of space [4, 5, 6, 7]. In recent years, the focus on elastic and acoustic metamaterial theory and design has broadened to include non-reciprocal wave propagation [8], acoustic lenses [9], and optimal wave-absorbing layered media [10].

In many applications, the design of metamaterials for wave control is often a heuristic process, which encourages heavy optimisation and machine learning techniques in the literature [11, 12]. However, even after long and extensive computations to find an optimal metamaterial arrangement, small manufacturing changes/defects can lead to errors that significantly alter the band structure. For this reason, these materials require elaborate manufacturing techniques [13, 14].

One possible strategy to achieve multiple band gaps is to combine different types of sub-wavelength resonators, each with a different resonance frequency. However, to date there has been no clear strategy or simple formula for the effective properties of a mix of different types of resonators. It has only been possible to derive the effective properties of a periodic array of identical sub-wavelength resonators [15, 16, 17].

In this paper, we present a disordered (random) metamaterial, which can be designed to have broad as well as multiple localised (overlapping) low-frequency band gaps, that are robust to small changes in its microstructure. We show how to design such metamaterials and, importantly, derive simple explicit formulae for the band gaps which do not require heavy optimisation. We achieve this by combining ensemble averaging techniques [18, 19, 20] together with asymptotic homogenisation.

In disordered materials, it is more straightforward to add a mix of resonators, with the simplest case being just a uniform random mix of the resonators. In terms of fabrication, the main difficulty is to make the resonators themselves and not to precisely place them. The drawback of disordered materials is that their scattering response from any one configuration of these resonators is complicated. In this paper, we greatly simplify this complication by taking an ensemble average: that is, we calculate the average wave by averaging over all possible positions and properties of the resonators. As a result, a band gap in this context is where the average wave transmission is approximately zero, but there may still be some transmission in the form of a completely speckled wave [21].

In this paper, we use as an example a split-ring resonator, shown in Figure 1a, because its scattered wave has been deduced from first principles [22, 23, 15]. It is a type of Helmholtz resonator, characterised by a cavity-neck system with resonance peak located in the sub-wavelength range ($kb \leq 1$), shown in Figure 1b. An example of using split-ring resonators in a periodic lattice is deduced in [22, 16, 17].

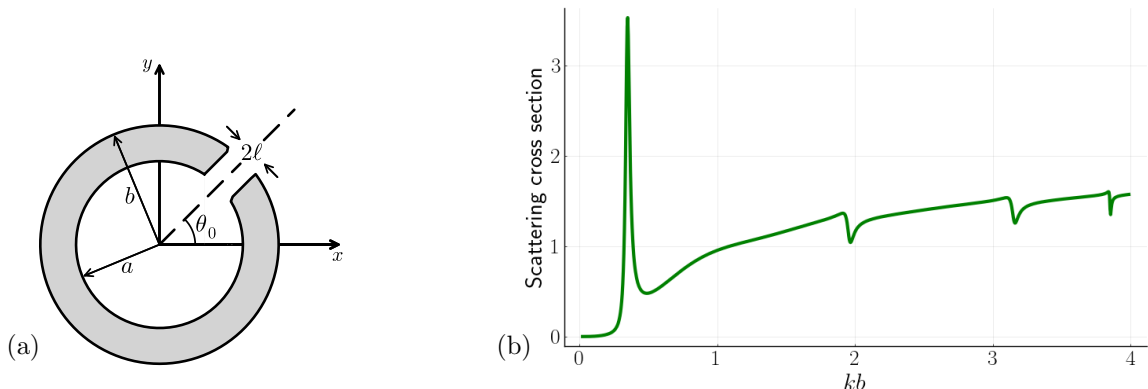


Figure 1: The left figure (a) shows an illustration of a typical split-ring resonator. The right figure (b) shows the scattering cross section of a sound-hard 2D split-ring resonator with an aperture size of $2\ell = 0.1b$, and k is the wavenumber of the background medium.

To reach simple formulae, which are needed to easily design materials, asymptotic homogenisation is essential [15, 24, 25, 26, 27]. It is typically used to enforce that the resonators are sub-wavelength, as we also do in this work. However, care must be taken to accurately capture the resonance.

To showcase the design process using our formulae, and motivate the reader for the rest of the paper, we present an acoustic version of a device that splits a signal into two different channels, or waveguides, dependent on its frequency components shown in Figure 2. These devices are known as frequency demultiplexers. They are used in digital computing and telecommunication networks, and are often designed via tailored periodic structures, as in [28], or through black-box optimisation, as in [29]. In contrast, as illustrated in Figure 2, we are able to produce with little effort a low insertion loss ($\lesssim 5\text{dB}$) and high contrast ($\sim 10 - 20\text{dB}$) demultiplexer using only randomly placed and oriented resonators, which has similar performance compared to the microchip in [29, figure4b].

Designing devices, such as the demultiplexer in Figure 2, with randomly oriented resonators makes them robust to manufacturing defects in terms of the positioning of each resonator. This is because the formulae for the effective-properties are agnostic to the position and orientation of the resonators. Alternatively, the performance could be further enhanced by optimising the position of the resonators.

2 Results

In this section, we present our main results: the effective-properties of the metamaterial. Later, in Section 3.3, we show how to derive these results. The focus below is on how to use the effective-properties, followed by examples, and to present high-fidelity Monte-Carlo validation.

The resonators in the material can have varied sizes, geometry, and properties, although for ease of exposition we illustrate the case of circular sound-hard split-ring resonators in 2D, as shown in Figure 3. Let us consider N different types of sound-hard Helmholtz resonators, which are randomly distributed in a

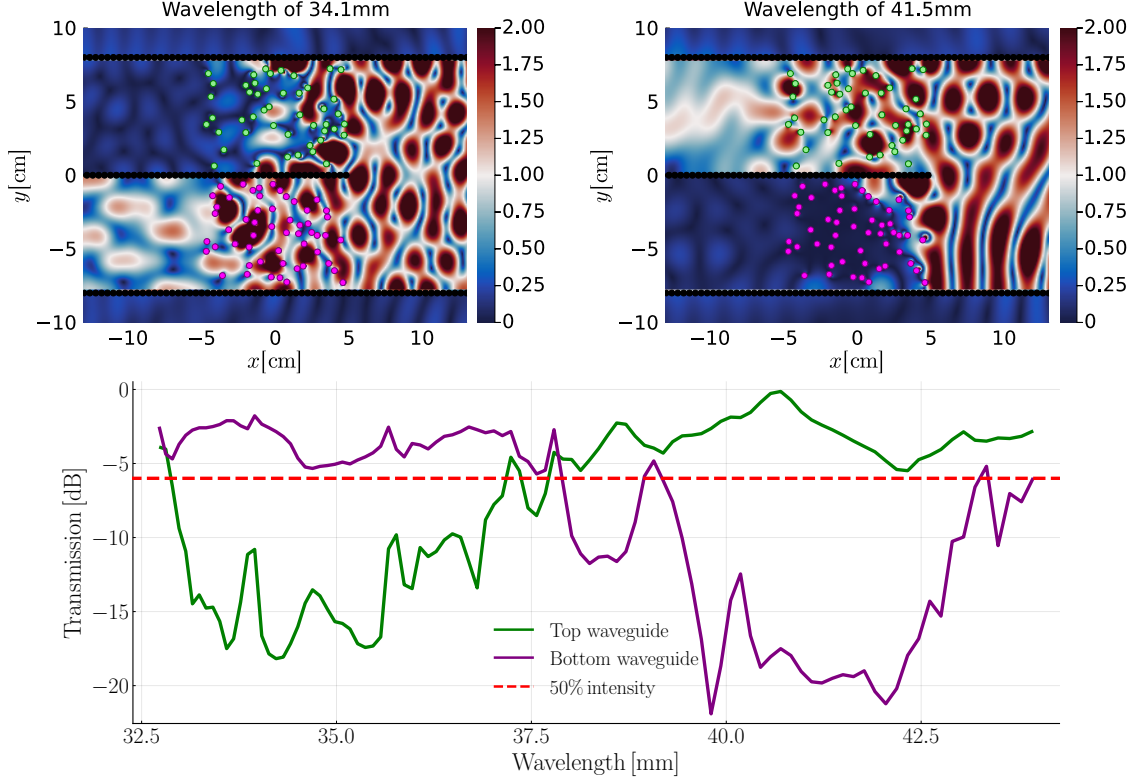


Figure 2: The top two images show a very simple frequency demultiplexer we designed using Helmholtz resonators to illustrate our results. In both images an incident planar wave (of amplitude 1) travels from right to left inside a waveguide which gets split into two waveguides at $x = 5\text{cm}$. The top waveguide filters out waves with wavelengths close to 34.1mm due to the scattering by resonators represented by green circles, with an aperture of $2\ell = 0.2\text{mm}$. Likewise, the bottom waveguide filters out waves with wavelengths close to 41.5mm due to the scattering by resonators represented by magenta circles, with an aperture of $2\ell = 0.04\text{mm}$. All resonators are thin-walled ($a = b = 2\text{mm}$ in Figure 1a) and solid, randomly placed and oriented in air at the entrance of each waveguide. The colour bar shown is the amplitude of the total wave (incident plus scattered). The graph below shows the transmitted intensity by each waveguide in dB. Wavelengths from 33 to 38mm are mostly transmitted through the lower waveguide, while wavelengths from 38 to 43mm are mostly transmitted through the upper waveguide.

homogeneous background medium (see Figure 3). The properties of the resonators feed into the formulae for the effective bulk modulus (β_*) and effective mass density (ρ_*), which are given by:

$$\beta_*(k) = \frac{\beta}{(1 - \varphi) + \sum_{j=1}^N z(\lambda_j)\phi_j} \quad \text{and} \quad \rho_* = \rho \frac{1 + \varphi}{1 - \varphi}, \quad (1)$$

where β and ρ are the bulk modulus and mass density of the background medium, ϕ_j is the volume fraction of the j -th type of resonator¹, with $\varphi = \sum_{j=1}^N \phi_j$ being the total volume fraction of the resonators (including their interiors). We call $z(\lambda_j)$ the *resonance factor* of the j -th resonator type derived via careful matched asymptotic analysis [22, 16]. The resonance factor depends only on the geometrical properties of the resonator and the wavenumber k of the background medium. When hitting a resonance $z(\lambda_j)$ increases in magnitude, and when there is no contribution from the resonator then $z(\lambda_j)$ is small. See Section 3.1 for more details and see Appendix A for a derivation of a formula for $z(\lambda_j)$ for split-ring resonators.

The effective bulk modulus β_* is frequency-dependent, and its behaviour depends on the geometry of each resonator in the mixture. $\beta_*(k)$ is the most important parameter to design band gaps for metamaterials, since

¹For two dimensions, the volume fraction reduces to the ratio of the area occupied by a phase to the total area of the material.

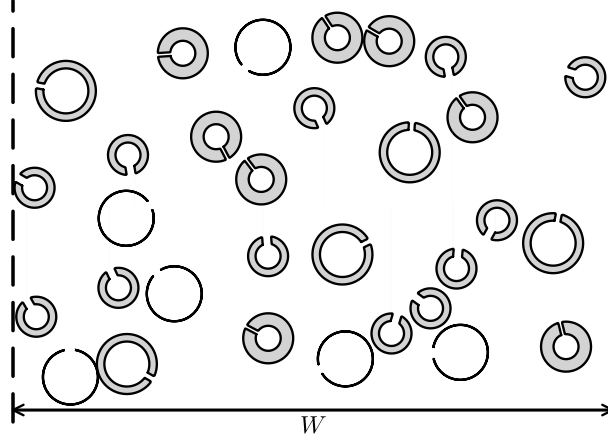


Figure 3: Representation of one possible configuration of split-ring resonators in a layer of width W .

the effective mass density ρ_* does not depend on frequency and only increases when adding more resonators to the mixture.

Below we show three examples on designing band gaps by using the formulae above. After the examples, we show how high-fidelity Monte-Carlo simulations closely agree with our simple formulae for a broad frequency range.

2.1 Example band gap designs

In this section we present three examples to show how to design band gaps using a layer of randomly placed resonators, as illustrated in Figure 3. For all the examples we assume that the background medium is air ($\rho = 1\text{kg/m}^3$, $\beta = 117.6\text{kPa}$).

Example 1 – changing volume fractions. Consider a material filled with a single species of thin-walled split-ring resonator ($a = b$ and one fixed value of the aperture 2ℓ in Figure 1a). To help illustrate the results, we consider a layer of width W (infinite length), shown in Figure 3, and calculate its effective transmission coefficient by assuming the material is homogeneous with the properties given by (1).

From the results, shown in Figure 4b, we see that only a small percent of resonators are needed to completely stop transmission through this layer. As the volume fraction increases, the minimum grows wider and shifts towards higher frequencies. With only $\varphi = 6\%$ volume fraction, we reach a band gap around 140Hz, which shows that a thin layer of the proposed metamaterial is a good candidate for a sound-insulating material. To broaden the band gap, it is possible to either increase the width of the metamaterial layer W , or the volume fraction of resonators φ (see Figure 4b).

Another lesson to learn from Figure 4a is that the minimum of the curve $\varphi = 1\%$ is very close to the resonance frequency of a single thin-walled resonator, shown in (1)b. However, the minimum of $\text{Im}[\beta_*]$ the curves shifts to higher frequencies as φ increases because of multiple scattering effects between the resonators. Being able to predict this minimum, with our formulae (1), rather than finding it through trial and error, can save time and resources in most applications.

Finally, because Figure 4a has non-dimensional independent variables, note that increasing the size of the resonators, while thickening their walls, would lead to the band gap shifting to a lower frequency range.

Example 2 – broadening band-gaps. To achieve a broader band gap, or separate band gaps, we could use layers of random resonators of the type discussed in Example 1. Instead, we show a case with two types of thin-walled resonators to the formulae (1) with multiple types of resonators. The two types have different radii, $b_1 \neq b_2$, and aperture sizes, $\ell_1 \neq \ell_2$. The results are presented in Figure 5.

In Figure 5(a) we notice that when the aperture ℓ_2 decreases, the graph of $\text{Im}[\beta_*]$ transitions from having one minima to two distinct minima. The appearance of the second dip is due to the resonance frequencies of the two types of resonators moving further apart as we decrease ℓ_2 . The overall result in the transmission (Figure 5b) is a wide band gap, which separates into two thinner band gaps as ℓ_2 decreases.

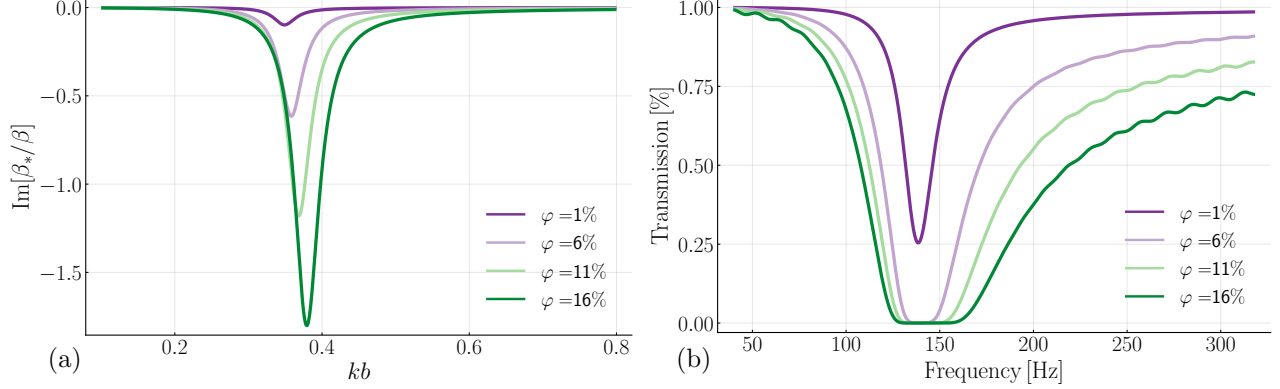


Figure 4: (a) shows the imaginary part of the effective bulk modulus β_* and (b) the magnitude of the transmission coefficient through a layer of width $W = 32\text{mm}$. The layer is composed of thin-walled randomly-positioned Helmholtz resonators with radius $b = 0.4\text{mm}$, and k is the background wavenumber. The aperture size of the resonators is $\ell = 0.05b$. Each curves has a different volume fraction of resonators.

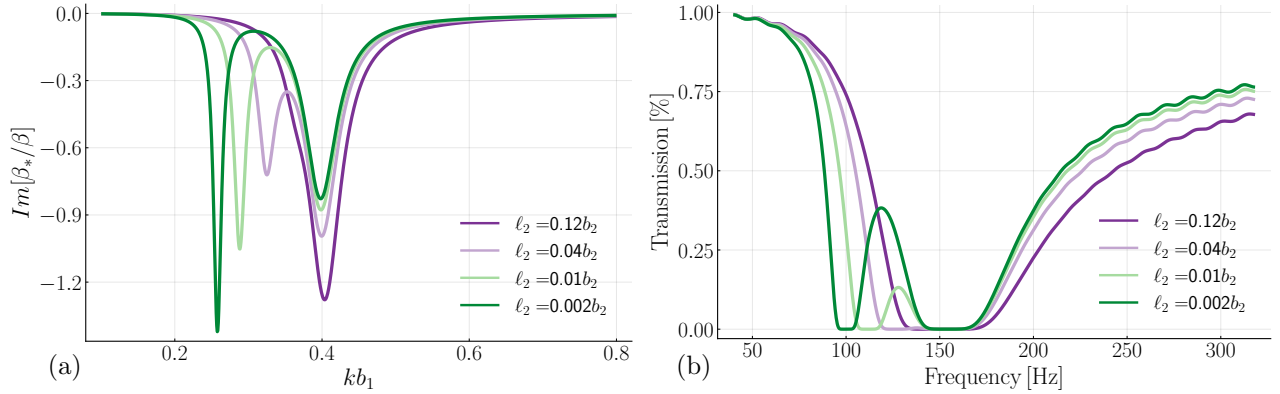


Figure 5: (a) shows the imaginary part of the effective bulk modulus and (b) shows the magnitude of the transmission coefficient through a layer of width $W = 32\text{mm}$. The layer is composed of thin-walled random Helmholtz resonators with radius $b_1 = 0.4\text{mm}$ and $b_2 = 0.2\text{mm}$. The total volume fraction of resonators is $\varphi = 15\%$, and half of them ($\phi_1 = 7.5\%$) have an aperture size of $\ell_1 = 0.1b_1$. Only the aperture size ℓ_2 of the other half of the resonators changes between curves.

Example 3 – shifting band-gaps. Here we consider a mix of three types of resonators, each with a volume fraction of $\phi_j = 4\%$ for $j = 1, 2, 3$. We use three types just to show case that we can. Each resonator has a different aperture size, but the three types have the same outer and inner radius b and a , for simplicity. Our goal is to show how the band-gaps shift when the wall of the resonators become thicker. Increasing the thickness causes a non-intuitive change in the resonance which can only be predicted with our effective properties (1).

The transmission results for different values of the inner radii a , which changes the wall thickness, are shown in Figure 6 below. In Figure 6a we see that as a gets smaller, and the wall thickness increases, the resonant frequency gets lower, however there is a limit to this effect. In Figure 6b we see that a further decrease in a makes the resonant frequency become higher again, as well as lessening the strength of the resonance. These effects illustrate the need for our formulae to guide the design process.

2.2 Monte-Carlo validation

When dealing with disordered materials it is often impractical to predict the precise wave response of the material for each possible configuration of the microstructure. To reach our effective formulae (1) we used ensemble averaging techniques [30], which lead to practical and explicit results. In this section we validate

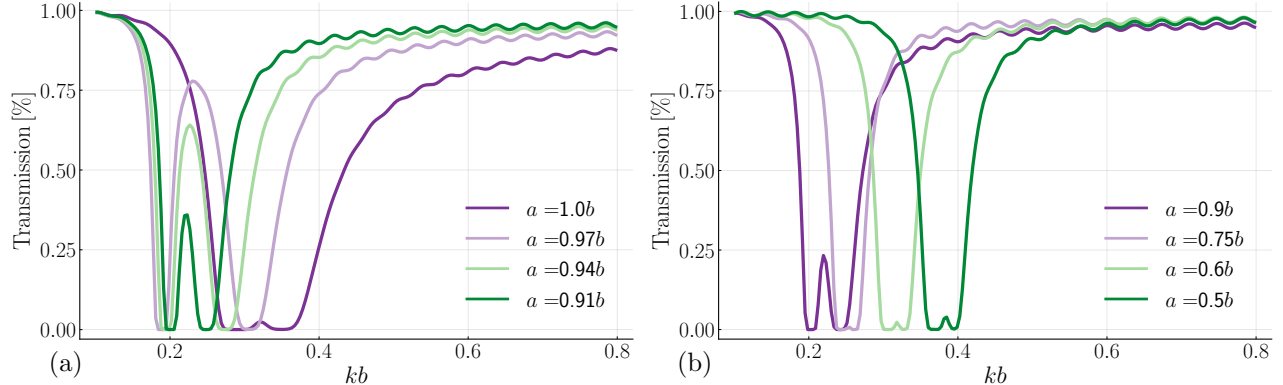


Figure 6: Both graphs show the transmission coefficient through a metamaterial of width $W = 32\text{mm}$ filled with randomly positioned resonators, all with the same outer radius b . The total volume fraction of resonators is $\varphi = 12\%$, with a third of them having an aperture size of $\ell_1 = 0.05b$, another third with $\ell_2 = 0.01b$, and the final third with $\ell_3 = 0.005b$. For each curve we use a different inner radius a for all the resonators.

these formulae by using high-fidelity Monte-Carlo simulations for both a layer and circle filled with resonators. We also highlight some advantages and disadvantages of disordered metamaterials in general.

To get an exact match with a high-fidelity simulation, we need to perform simulations of wave scattering from one configuration at a time, where the resonators do not overlap and their positions are randomly chosen, see [31] for details. The average wave is then calculated by taking the average total wave over all simulations. This is what we mean by a high-fidelity Monte-Carlo simulation. The mathematical details on ensemble averaging and Monte-Carlo method are given in Section 3.2; here we focus mostly on showing the results.

A layer filled with resonators

We begin with the case of a layer filled with resonators and an incident plane wave. This is a case which is simpler to understand, though Monte-Carlo simulations can be challenging as the layer needs to be very tall, large H in Figure 7, as the effective theory assumes the layer is infinitely tall.

We perform a high-fidelity Monte-Carlo simulation for a plane incident wave, with wavenumber k , scattered by randomly distributed and randomly oriented split-ring resonators ($b = a$ in Figure 1a) inside a long strip shown in Figure 7a. The transmitted field is measured one radius away from the layer as also illustrated in Figure 7a. This simulation is repeated many times, and the average transmission is compared with the prediction from the effective-properties formulae (1) in Figure 7b below. The runtime of the MC simulation was over 24 hours, with parallelization, and using all computational power available, while the effective formulas are computed in a few seconds, using only a fraction of the computational power.

In Figure 7b we see that the transmission calculated using the effective-properties (1) accurately matches the average from Monte-Carlo (MC) in the frequency range $kb \lesssim 0.4$ which includes the resonant frequencies², which agrees with our derivations in Section 3.3. The MC mean intensity is higher than the MC mean amplitude, specially around resonance, due to there being no phase cancellation when calculating the mean intensity. Another way to see this is that, in each Monte-Carlo realisation, part of the field has become incoherent or speckled due to scattering [21]. This incoherent part is lost when taking the average of the field, due to phase cancellation, but not in the average intensity.

²Note that some MC points between $kb = 0.08$ and $kb = 0.22$ are higher than 100% due to diffraction from the corners of the layer, given it has a finite height.

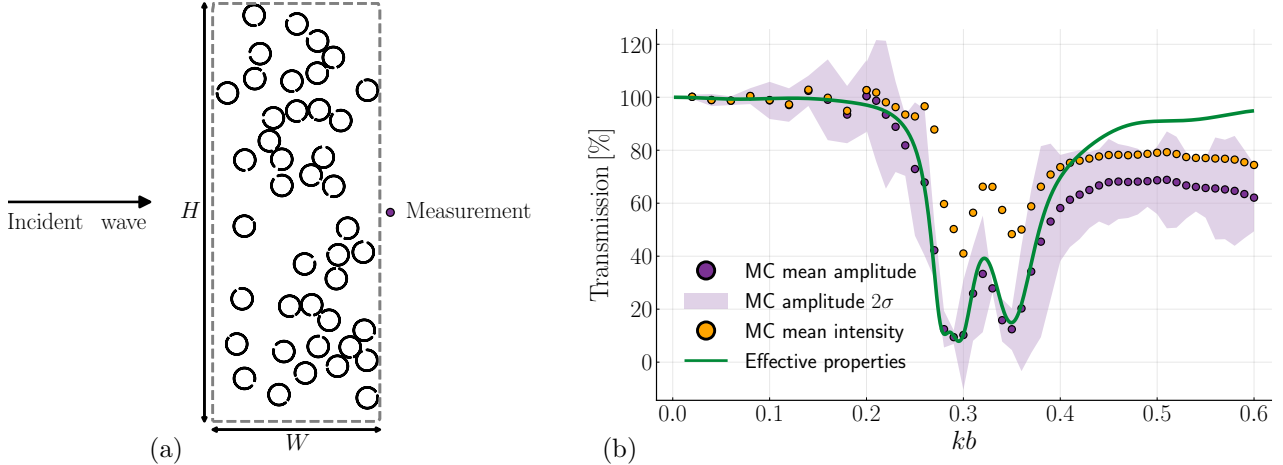


Figure 7: (a) shows one realisation used for our Monte-Carlo (MC) simulations, where resonators are placed within a layer of width $W = 20b$, height $H = 200b$, and b is the resonator radius. An incident plane wave comes from the left and the total field is then measured at a point at half height and one radius away from the layer. This simulation is repeated many times, each with a different configuration of resonators, and then the average MC field is compared with a transmission coefficient calculated by using the effective-properties (1), shown on the right (b). For the MC we use three types of thin-walled resonators, each with 4% volume fraction, but with different aperture sizes $\ell_1 = 0.05b$, $\ell_2 = 0.01b$, and $\ell_3 = 0.005b$. In total 5,000 different configurations are calculated for the MC results in (b), and σ is the $2\times$ the standard deviation.

An important feature from Figure 7b is that each realisation of the Monte-Carlo simulation is close to the MC mean amplitude. That is, the purple shaded area has a 95% statistical confidence (2σ). This suggests a powerful design strategy: 1) first use the effective formulae to decide on what types of resonators to use, given some target band diagram, then 2) produce one realisation with the resonators randomly placed, and finally 3) perform a local optimisation to adjust the position of the resonators to further refine the transmission or reflecting properties. This design strategy would be much less computationally intensive than pure optimisation strategies used in the literature [11, 12, 29], as we discussed in Section 1.

A circle filled with resonators

Our effective formulae (1) are valid for materials of any shape [19, 32]. In particular, a circle filled with resonators leads to finite size Monte Carlo simulations (MC) [32, 33] which makes validation far simpler. See Figure 8a for an illustration.

Our goal here is to compare three different methods to calculate the scattering cross section of a circle filled with resonators: 1) MC simulations, 2) a circle with the effective properties (1), and 3) the effective waves methods [19, 32] which works beyond low frequencies. The results are shown in Figure 8b. The runtime of the MC simulation was over 5 hours, with parallelization, and using all computational power available. The effective waves method and effective formulas are computed in over 40 minutes and a few seconds respectively, using only a fraction of the computational power.

When performing MC for a circle filled with resonators, we make use of the rotational symmetry to greatly reduce the computational cost of calculating the scattering cross section, see [33] for details. For the circle with either effective properties, or using the effective waves methods [19, 32], the scattering cross section becomes:

$$\langle \Sigma_{sc} \rangle = \frac{2}{kR} \sum_{n=-\infty}^{\infty} |\langle \mathcal{F}_n \rangle|^2, \quad (2)$$

where R is the radius of the metamaterial, and $\langle \mathcal{F}_n \rangle$ are the average material coefficients defined in Section 3.2.

The results in Figure 8b again show that the mean of MC data is close to the results using the simple formulae for the effective-properties at lower frequencies $kb \lesssim 0.7$. The effective-properties are deduced as a low-frequency asymptotic approximation of the effective waves method, and it can be seen in Figure 8 that

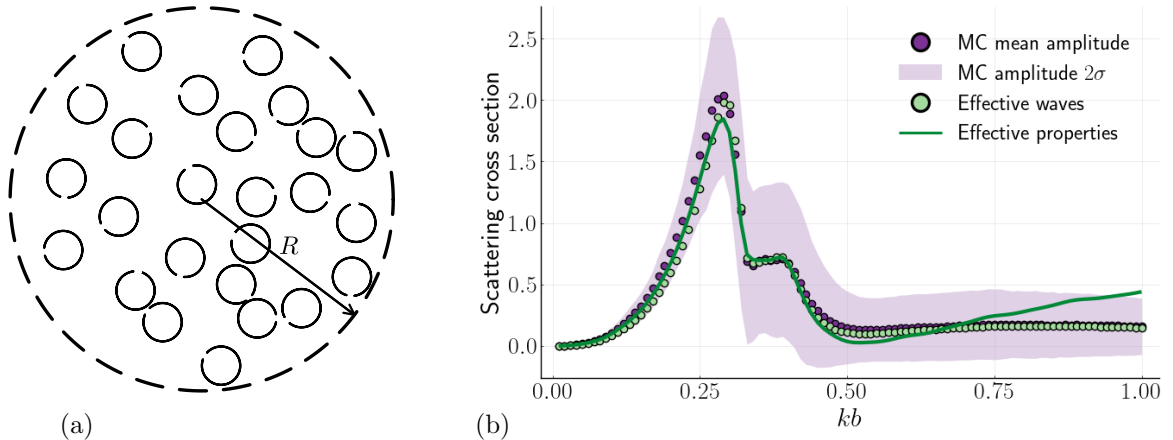


Figure 8: (a) shows one configuration of resonators used for our Monte-Carlo (MC) simulations. The resonators are placed randomly within a circle of radius $R = 20b$. An incident planar wave comes from the left and the resulting scattering cross section is shown in (b) on the right for three different methods: MC simulations, the effective waves method [19], and by using the effective-properties (1). The aperture size of all resonators is $\ell = 0.05b$, the volume fraction is $\varphi = 10\%$ in all 40,000 configurations of the MC simulations, and σ is the standard deviation².

these two methods match for lower frequencies. We can also see that the effective waves method matches the Monte-Carlo results for all frequencies. However, the effective waves method has a significant drawback: it requires a much more elaborate calculation [32] than the formulae (1), which makes it less useful than the effective formulae for designing metamaterials.

3 Multiple scattering and ensemble average

Here we derive the effective-properties (1) in three steps: scattering by a single resonator in Section 3.1, scattering of the whole metamaterial in Section 3.2, and then an asymptotic low-frequency expansion in Section 3.3.

3.1 Scattering by a single resonator

Before calculating the acoustic response of the whole metamaterial, we need to describe how each resonator scatters waves. This is best done with the T-matrix method [34, 35, 36], which we describe below, as it facilitates calculations for multiple scattering.

Let the centre of the resonator be the origin of \mathbb{R}^2 . We assume the incident wave is a regular function, which allows us to expand the incident wave in terms of a series of regular radial waves:

$$u_{\text{inc}}(\mathbf{r}) = \sum_{n=-\infty}^{\infty} g_n V_n(k\mathbf{r}) \quad \text{with} \quad V_n(k\mathbf{r}) = J_n(kr) e^{in\theta}, \quad (3)$$

where $\mathbf{r} \in \mathbb{R}^2$, k is the wavenumber, J_n being the Bessel function of the first kind, and (r, θ) polar coordinates of \mathbb{R}^2 . Note that the time-harmonic dependence $e^{-i\omega t}$ is assumed throughout the paper for both incident and scattered waves, where ω is the angular frequency, and $k = \omega/c$, where c is the speed of sound in the background medium.

Due to the linearity of the Helmholtz equation, the total field is given by the superposition of the incident wave and the scattered field from our resonator:

$$u_{\text{tot}}(\mathbf{r}) = u_{\text{inc}}(\mathbf{r}) + u_{\text{sc}}(\mathbf{r}),$$

²The scattering cross section (2) was calculated with the first nine scattering coefficients $\langle \mathcal{F}_n \rangle$ in (2).

and, outside the resonator, the scattered field can be represented as a series of outgoing radial modes:

$$u_{\text{sc}}(\mathbf{r}) = \sum_{n=-\infty}^{\infty} f_n U_n(k\mathbf{r}), \quad \text{for } r = |\mathbf{r}| > b, \quad (4)$$

where b is the outer radius of the resonator, f_n are the scattering coefficients, and the outgoing radial modes are given by:

$$U_n(k\mathbf{r}) = H_n(kr) e^{in\theta},$$

with H_n being the Hankel function of the first kind³.

To determine the scattered field, we need to apply boundary conditions at the walls of the resonator. The result of solving the boundary conditions can be expressed in terms of the T-matrix which relates the incident wave to the scattered waves through:

$$f_n = \sum_{m=-\infty}^{\infty} T_{nm} g_m, \quad (5)$$

where T_{nm} are the elements of the T-matrix. For a circular Helmholtz resonator with sound-hard walls (Neumann boundary conditions) and outer radius b , we deduce in Appendix A the T-matrix:

$$T_{np} = -\frac{J'_p(kb)}{H'_p(kb)} \delta_{np} - \frac{ie^{-i(n-p)\theta_0}}{\pi H'_n(kb) H'_p(kb)} z(\lambda), \quad (6)$$

where θ_0 is the orientation of the aperture (anticlockwise angle with the x -axis), prime denotes differentiation with respect to the argument, and λ is a set of properties that identifies one type of resonator.

In Appendix A we use a closed form for $z(\lambda)$ for the split-ring resonator in Figure 1 which is fully characterised by $\lambda = \{kb, ka, k\ell\}$, with outer radius b , inner radius a , and aperture of ℓ . However, the formula (6) is the same for any circular resonant structure, with only $z(\lambda)$ changing, with some examples illustrated in Figure 9.

To determine the resonance factor $z(\lambda)$ for a different resonator, one should redo the asymptotic calculations in [22] for its specific internal geometry, and then repeat the deduction in Appendix A to arrive at (6). Similarly, we could easily adapt (6) to incorporate the case of multiple apertures in the same resonator.

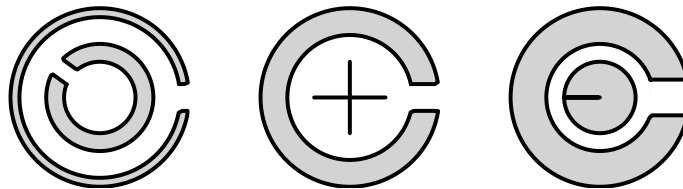


Figure 9: Three examples of Helmholtz resonators with different resonance factors $z(\lambda)$.

3.2 Ensemble average and multiple scattering

To account for different types of resonators in the metamaterial we need to first calculate the exact multiple scattering between the resonators, after which we will perform ensemble averaging as shown in [19, 33, 36]. We also borrow the notation from these references.

Let us number each resonator in the material. We denote the centre of the j -th resonator by \mathbf{r}_j , and the set of its properties by λ_j . As an example, if the j -th resonator is a split-ring resonator, shown in Figure 1, we have the following set of properties:

$$\lambda_j = \{kb_j, ka_j, k\ell_j\}$$

where b_j is the outer radius, a_j the inner radius, and ℓ_j the aperture size.

³The usual superscript (1) on the Hankel function is suppressed here and henceforth for clarity.

The scattered field from all resonators is a sum of the waves scattered from each resonator:

$$u_{\text{sc}}(\mathbf{r}) = \sum_{j=1}^J \sum_{n=-\infty}^{\infty} f_n^j U_n(k\mathbf{r} - k\mathbf{r}_j), \quad (7)$$

where \mathbf{r} can not be within any resonator, J is the total number of resonators, and f_n^j are the scattering coefficient of the j -th resonator as introduced in Section 3.1.

For numerical validation, and to help explain the ensemble averaging, it helps to specialise to the case of all resonators within a large sphere. To achieve this we use Graf's addition theorem, to rewrite (7) in terms of outgoing waves centred as the origin:

$$u_{\text{sc}}(\mathbf{r}) = \sum_{j=1}^J \sum_{n,n'=-\infty}^{\infty} V_{n-n'}(-k\mathbf{r}_j) f_n^j(\Lambda) U_{n'}(k\mathbf{r}). \quad (8)$$

The coefficients f_n^j depend on all properties and positions of all the resonators [19, 36]. To make this explicit, and simplify notation, we denote one configuration by Λ , which represents all the positions and properties of the resonators. We also define the material scattering coefficients of the whole sphere containing all the resonators as:

$$\mathcal{F}_n(\Lambda) = \sum_{j=1}^J \sum_{n'=-\infty}^{\infty} V_{n'-n}(-k\mathbf{r}_j) f_{n'}^j(\Lambda),$$

which simplifies (8) into:

$$u_{\text{sc}}(\mathbf{r}) = \sum_{n'=-\infty}^{\infty} \mathcal{F}_n(\Lambda) U_n(k\mathbf{r}). \quad (9)$$

To calculate the average response of the metamaterial, we ensemble average over all possible positions, orientations and properties [19, 20, 30], while assuming that resonators do not overlap, and that any possible configuration Λ_i has the same probability (micro-canonical ensemble), which results in:

$$\langle u_{\text{sc}}(\mathbf{r}) \rangle = \frac{1}{M} \sum_{i=1}^M \sum_{n=-\infty}^{\infty} \mathcal{F}_n(\Lambda_i) U_n(k\mathbf{r}) = \sum_{n=-\infty}^{\infty} \langle \mathcal{F}_n \rangle U_n(k\mathbf{r}), \quad (10)$$

where the bracket notation $\langle \circ \rangle$ denotes the ensemble average of \circ , and M is the number of possible configurations Λ_i which tends to infinite.

The average material coefficients $\langle \mathcal{F}_n \rangle$ can be calculated either by the effective waves method [19, 33], or by brute force Monte-Carlo simulations using the Julia library MultipleScattering.jl [37].

The effective waves method calculates the average amplitude (10) directly, avoiding the explicit computation of the scattering from each configuration (9). Further, this method provides a semi-analytic formula for the dispersion equation of the meta-material, which we use to obtain a low-frequency expansion in Section 3.3, resulting in explicit formulae for the effective-properties.

On the other hand, Monte-Carlo simulations estimate the average response by explicitly calculating the scattering from each configuration Λ_i , and then repeating this for a very large number of possible configurations, and then calculate the average (10). This strategy also allows the computation of higher statistical moments of the scattered field, such as the mean scattered intensity:

$$\langle |u_{\text{sc}}(\mathbf{r})|^2 \rangle = \sum_{n,m=-\infty}^{\infty} \langle \mathcal{F}_n^* \mathcal{F}_m \rangle U_n^*(k\mathbf{r}) U_m(k\mathbf{r}), \quad (11)$$

where $*$ means complex conjugation. In Section 2.2 we used both the mean amplitude (10) and mean intensity (11) calculated from Monte-Carlo simulations for our disordered metamaterial, and compare them against the average response from the effective-properties (1) deduced in Section 3.3 that follows.

3.3 low-frequency expansion

In this section, we use the dispersion equation for a 2D random particulate material from the effective waves method in [33, equation 4.10] to derive effective-properties of the metamaterial with resonators. As we are interested in the long wavelength regime, we assume that the resonators' positions, orientations, and properties are uncorrelated, except that the resonators can not overlap⁴. For these assumptions, the dispersion equation [33, equation 4.10] simplifies into:

$$F_m(\lambda_1) + \sum_{n'=-\infty}^{\infty} \frac{2\pi\bar{T}_n(\lambda_1)}{k_*^2 - k^2} \int N_{n'-m}[k(b_1 + b_2), k_*(b_1 + b_2)] F_{n'}(\lambda_2) \mathbf{n}(\lambda_2) d\lambda_2 = 0, \quad (12)$$

where $N_n[x, y] = xH'_n(x)J_n(y) - yJ'_n(y)H_n(x)$, $\mathbf{n}(\lambda)$ is the number density of resonators of type λ , k_* is the effective wavenumber, $\bar{T}_n(\lambda)$ is the isotropic T-matrix (25) derived in Appendix A, and F_n is the amplitude of the effective wave, defined in [33].

We define the effective speed of sound as follows:

$$c_* = ck/k_*.$$

To do an asymptotic expansion, we assume there is a maximum outer radius for the resonators b_{\max} , such that $b_j \leq b_{\max}$ for all j . We also recall that all resonators are sub-wavelength, so the dimensionless wavenumber $\epsilon = kb_{\max}$ is small. Then, we expand both the speed of sound and effective wavenumber as a power series of ϵ :

$$\frac{c}{c_*} = \chi + \mathcal{O}(\epsilon) \quad \text{and} \quad k_* b_j = \chi \alpha_j \epsilon + \mathcal{O}(\epsilon^2), \quad (13)$$

where $\alpha_j = b_j/b_{\max}$, and χ has yet to be determined.

To determine χ we need to do an asymptotic expansion of the terms in (12), including $\bar{T}_n(\lambda_1)$ which depends on the resonance factor. The trick to do this elegantly is to make no assumptions about the asymptotic order of $z(\lambda)$. This is because $z(\lambda)$ depends on the frequency in a non-trivial way, involving all parameters of the resonators internal geometry (see (26) and (27) in Appendices A and B). Fortunately we can reach simple formulae without making any assumption about $z(\lambda)$. Instead, the results error of our method will be relative to $z(\lambda)$.

Performing an asymptotic expansion on the terms in (12) results in:

$$\begin{aligned} \frac{1}{k_*^2 - k^2} &= \frac{b_{\max}^2}{\chi^2 - 1} \frac{1}{\epsilon^2} + \mathcal{O}(\epsilon^{-1}), \\ N_{n'-m}(kb_{1,2}, k_* b_{1,2}) &= N_{n'-m}^{(0)}(\chi) + \mathcal{O}(\epsilon), \quad \text{with } N_n^{(0)}(\chi) = \frac{2i}{\pi} \sum_{m=-\infty}^{\infty} \chi^{|m|} \delta_{n,m}, \\ \bar{T}_n(\lambda_1) &= \bar{T}_n^{(2)}(\lambda_1) \alpha_1^2 \epsilon^2 + \mathcal{O}(\epsilon^3(1 + z(\lambda))), \quad \text{with} \\ \bar{T}_n^{(2)}(\lambda_1) &= \frac{i\pi}{4} [\delta_{n,1} + \delta_{n,-1} - \delta_{n,0} + z(\lambda_1) \delta_{n,0}]. \end{aligned} \quad (14)$$

where $\delta_{n,m}$ is the delta Kronecker symbol. We have included $z(\lambda)$ in the error so that we do not need to make assumptions about the size of $z(\lambda)$ which can be large. Fortunately, this works well, as the maximum relative error of the leading order term for \bar{T}_n is ϵ . We see this trend in the numerical validation.

Substituting (14) into (12), and retaining only the leading order terms we reach:

$$F_n(\lambda_1) - \frac{2\pi b_{\max}^2}{1 - \chi^2} \bar{T}_n^{(2)}(\lambda_1) \alpha_1^2 \sum_{n'=-1}^1 N_{n'-n}^{(0)}(\chi) \int F_{n'}(\lambda_2) \mathbf{n}(\lambda_2) d\lambda_2 = 0, \quad (15)$$

where the sum is truncated to three terms as the other terms are of higher order in ϵ . To determine χ we

⁴To reach a dispersion equation we also need a closure assumption. We use the Quasi-Crystalline Approximation discussed in [38, 20].

multiply both sides of (15) by $\mathbf{n}(\lambda_1)$ and integrate over λ_1 , leading to the following eigenvalue problem:

$$\sum_{n'=-1}^1 M_{nn'} \tilde{F}_{n'} = 0, \quad \text{with} \quad \tilde{F}_n = \int F_n(\lambda_1) \mathbf{n}(\lambda_1) d\lambda_1 \quad \text{and} \quad (16)$$

$$M_{nn'} = \delta_{n,n'} - \frac{2\pi b_{\max}^2}{1 - \chi^2} N_{n'-n}^{(0)}(\chi) \int \bar{T}_n^{(2)}(\lambda_1) \alpha_1^2 \mathbf{n}(\lambda_1) d\lambda_1.$$

By solving the dispersion relation $\det M = 0$, we can obtain an exact expression for χ which substituted into (13) leads to (at leading order):

$$c_*^2 = \frac{\beta}{\rho} \frac{(1 - \varphi)}{\left(1 - \varphi + \sum_{j=1}^N z(\lambda_j) \phi_j\right) (1 + \varphi)}, \quad (17)$$

where, to simplify the exposition, we have specialised the above to a mixture of N types of resonators which led us to substitute

$$\mathbf{n}(\lambda) = \sum_{j=1}^N \frac{\phi_j}{\pi b_j^2} \delta(\lambda - \lambda_j), \quad (18)$$

where ϕ_j is the volume fraction of the resonator of type j , $\varphi = \sum_{j=1}^N \phi_j$ is the total volume fraction of resonators, and δ is the Dirac delta distribution.

Finally, we want an effective density ρ_* and bulk modulus β_* such that $c_*^2 = \beta_*/\rho_*$. Analogous to [18, 19] there is only one way to factor out β_* and ρ_* such that the limits $\phi_j \rightarrow 0$ are consistent, and they lead to (1) presented in Section 2. Then, to calculate the average response of any metamaterial, one can replace it with an effective homogeneous medium with properties given by (1). We validate these results against Monte-Carlo simulations in Figures 7 and 8.

We note that it is expected that Helmholtz resonators, with only one gap such as the examples shown in Figure 9, only significantly alter the effective bulk modulus, as we deduced in (1). This is because one gap leads to a dominant monopole term, and the monopole terms from the resonators contribute to the effective bulk modulus while the dipole terms contribute to the effective density. Therefore a dipole dominant resonator would lead to a significant change in the effective density.

4 Concluding remarks and further avenues

Summary. We have introduced a disordered composite metamaterial, consisting of sub-wavelength Helmholtz resonators. Having small resonators compared to the wavelength ($kb < 1$) allowed us to deduce, from first principles, formulae for both effective bulk modulus and effective mass density (1). These formulae were validated against high-fidelity Monte-Carlo simulations for both a layer and a circle filled with resonators. Using our effective formulae, we are able to quickly design broad frequency band gaps without using multiple layers, periodicity, or heavy optimisation methods. In future work, we plan to expand our results to higher order in kb and hence produce formulae that hold at higher frequencies, allow for effects of differing distributions of inclusions, and allow us quantify the difference between, say, random, periodic and hyperuniform materials.

Ensemble average properties. Contrary to the standard approach with periodic media, the formulae we deduce are based on ensemble averaging over the possible positions and orientations of the resonators, which introduces both advantages and disadvantages. The key advantages are that: 1) we were able to easily deduce effective-properties for any mix of different types of resonators, and 2) the effective properties are robust with respect to changes in position and orientation of the resonators, as shown by the motivation example in Figure 2. However, the effective properties in (1) do not give exactly the same results as any one specific configuration, and they also do not capture the average intensity of the scattered waves.

Applications. Despite using ensemble averaging in deriving (17), there are many applications for a single configuration of resonators. For example, the frequency demultiplexer in Figure 2 with only one configuration of resonator generated randomly had a similar performance compared with the one achieved via heavy optimisation in [29]. In part this is due to the response of a single configuration being close to the mean

response for low frequencies, as illustrated by the purple shaded region in Figures 7 and 8 which represents two standard deviations of the mean.

More general resonators. Throughout the whole paper we only showed examples of split-ring resonators from [22, 16, 17]. However, the formulae for the T-matrix (6) has the same form for any sub-wavelength circular Helmholtz resonator (which has one aperture), like the ones depicted in Figure 9, and the derived effective-properties (1) would have the same formula, although the resonance factor $z(\lambda)$ would change. Resonators with different internal structures should result in richer effective-properties for the metamaterial, as illustrated in Figure 6 for thick walled split-ring resonators.

Optimising band-gaps. One interesting direction to explore as future work is to implement the enhanced design strategy described in Section 2.2. This strategy consists of finding one specific configuration for the particles via optimisation while being guided by the overall band structure from the effective-properties (1).

Future generalisations. Another future avenue would be to investigate possible generalisations of the metamaterial presented. The simplest example is the three-dimensional case, where the Helmholtz resonators are spherical shells with a small aperture. Different from the case of long cylinders, small spheres could be used to produce compact versions of the metamaterial presented in three dimensions. Other than just acoustics, the case of sub-wavelength resonating structures in electromagnetism or elasticity could lead to interesting applications. For example, one could study how to embed sub-wavelength resonators in the building blocks of low-frequency operating machinery or other structures, to prevent harmful vibrations from propagating.

Acknowledgement

The author(s) would like to thank the Isaac Newton Institute for Mathematical Sciences, Cambridge, for support and hospitality during the programme Mathematical Theory and Applications of Multiple Wave Scattering, where work on this paper was undertaken. This work was supported by EPSRC grant EP/R014604/1. Paulo Piva gratefully acknowledges funding from an EPSRC Case studentship with Johnson Matthey. Art Gower gratefully acknowledges support from EPSRC (EP/V012436/1). David Abrahams gratefully acknowledges funding from the Royal Society for an Industry Fellowship with Thales UK.

Appendices

A Expression for the T-matrix

In this section, we deduce the T-matrix for a split-ring Helmholtz in (6) and use an expression for $z(\lambda)$ in (26) combined with (27) for a split ring resonator.

Consider a resonator with outer radius b , inner radius a , aperture size 2ℓ , and orientation θ_0 , as shown in Figure 1. Let us obtain the scattered field for the incident plane incident wave:

$$v_{\text{inc}}(\mathbf{r}) = e^{ikr \cos(\theta - \theta_{\text{inc}})},$$

Using [22, Equation (3.1)] we can calculate the scattered field for $\theta_0 = 0$ which in our notation becomes

$$v_{\text{sc}}(\mathbf{r}) = AU_0(k\tilde{\mathbf{r}}) + \sum_{n=-\infty}^{\infty} c_n U_n(k\mathbf{r}), \quad (19)$$

where $\tilde{\mathbf{r}} = \mathbf{r} - b(\cos(\theta_0), \sin(\theta_0))$ is the aperture location, c_n and A are coefficients given by [22, Eqs. (3.4) and (3.6) respectively]. To obtain the scattered field for $\theta_0 \neq 0$, we rotate the coordinate system $\theta \rightarrow \theta - \theta_0$, followed by the rotation of the incident wave $\theta_{\text{inc}} \rightarrow \theta_{\text{inc}} - \theta_0$. These rotations leave the incident wave unaltered while rotating the resonator by an angle of θ_0 which together with [22, Equation (3.1)] results in:

$$\begin{aligned} A &= -z(\lambda) \sum_{p=-\infty}^{\infty} \frac{i^p kb}{H'_p(kb)} e^{ip(\theta_0 - \theta_{\text{inc}})}, \\ c_n &= -i^n \frac{J'_n(kb)}{H'_n(kb)} e^{-in\theta_{\text{inc}}} - \frac{A Q_n(kb)}{2 H'_n(kb)} e^{-in\theta_0}, \end{aligned} \quad (20)$$

where $Q_n(x) = J_n(x)H'_n(x) + J'_n(x)H_n(x)$, the prime notation denotes the derivative with respect to the argument. We call the function $z(\lambda)$ the resonance factor and it is defined by (26) in Appendix B.

To rewrite (19) in terms of a T-matrix, shown in (5), we need to express all the terms centred at the origin, which leads us to use Graf's addition theorem to rewrite the monopole term evaluated at $k\tilde{\mathbf{r}}$ in the form:

$$U_0(k\tilde{\mathbf{r}}) = \sum_{n=-\infty}^{\infty} J_{-n}(kb)e^{in(\pi-\theta_0)}U_n(k\mathbf{r}),$$

which substituted into (19) leads to

$$v_{\text{sc}}(\mathbf{r}) = \sum_{n=-\infty}^{\infty} d_n U_n(k\mathbf{r}), \quad \text{with} \quad d_n = c_n + AJ_n(kb)e^{-in\theta_0}. \quad (21)$$

Next, the T-matrix (5) relates any incident wave to the scattered wave, so we need to rewrite any incident wave $u_{\text{inc}}(\mathbf{r})$ in terms of plane waves to use the results above. To achieve this, we use the Jacobi-Anger expansion of the plane wave:

$$v_{\text{inc}}(\mathbf{r}) = e^{ikr \cos(\theta-\theta_{\text{inc}})} = \sum_{n=-\infty}^{\infty} i^n J_n(kr)e^{in(\theta-\theta_{\text{inc}})},$$

followed by a superposition of plane waves:

$$\begin{aligned} u_{\text{inc}}(\mathbf{r}) &= \int_0^{2\pi} v_{\text{inc}}(\mathbf{r})g(\theta_{\text{inc}})d\theta_{\text{inc}} = \int_0^{2\pi} \sum_n g(\theta_{\text{inc}})i^n J_n(kr)e^{in(\theta-\theta_{\text{inc}})}d\theta_{\text{inc}} \\ &= \sum_n \left[i^n \int_0^{2\pi} g(\theta_{\text{inc}})e^{-in\theta_{\text{inc}}}d\theta_{\text{inc}} \right] V_n(k\mathbf{r}). \end{aligned} \quad (22)$$

Without loss of generality, we choose the amplitude of the packet of plane waves $g(\theta_{\text{inc}})$ in (22) such that:

$$i^n \int_0^{2\pi} g(\theta_{\text{inc}})e^{-in\theta_{\text{inc}}}d\theta_{\text{inc}} = g_n,$$

which implies that (22) now matches the form of any regular incident wave (3).

Now we need to perform the same operations on the scattered field v_{sc} (21) from a plane wave to obtain the total scattered field from any incident wave u_{sc} , which is possible due to the linearity of the Helmholtz equation and results in:

$$\begin{aligned} u_{\text{sc}}(\mathbf{r}) &= \int_0^{2\pi} v_{\text{sc}}(\mathbf{r})g(\theta_{\text{inc}})d\theta_{\text{inc}} = \sum_n \left[\int_0^{2\pi} d_n g(\theta_{\text{inc}})d\theta_{\text{inc}} \right] U_n(k\mathbf{r}), \\ &= \sum_{n,p} \left[-\delta_{np} \frac{J'_p(kb)}{H'_p(kb)} + \frac{2e^{-i(n-p)\theta_0}}{(\pi kb)^2 h(\lambda) H'_n(kb) H'_p(kb)} \right] g_p U_n(k\mathbf{r}), \end{aligned} \quad (23)$$

where we have used the Wronskian of Bessel-Hankel functions in the second line:

$$J_n(x)H'_n(x) - J'_n(x)H_n(x) = \frac{2i}{\pi x}.$$

Finally by comparing (5), (6) and (23) we conclude that:

$$T_{np} = -\frac{J'_p(kb)}{H'_p(kb)} \delta_{np} + \frac{ie^{i(n-p)\theta_0}}{\pi H'_n(kb) H'_p(kb)} z(\lambda), \quad (24)$$

which is the general T-matrix for a Helmholtz resonator using formulae in [22].

In Section 3.3, the T-matrix (6) is used to calculate the dispersion equation. However, as discussed in [19, 33], only the average T-matrix over all orientations of the aperture θ_0 contributes to the dispersion equation. We call this orientation averaged version of (6) the isotropic T-matrix, which is given by terms in the diagonal of (6), as follows:

$$\bar{T}_n(\lambda) = -\frac{J'_n(kb)}{H'_n(kb)} - \frac{iz(\lambda)}{\pi [H'_n(kb)]^2}. \quad (25)$$

B Low-frequency behaviour of the resonance factor

In this section we show $z(\lambda)$ for a 2D thin walled-split resonator. Other expressions for $z(\lambda)$ for other Helmholtz resonators can be deduced from [15, 39, 23]

We use the results from [22], where $z(\lambda)$ is related to the function $h(\lambda)$ through:

$$z(\lambda) = \frac{2i}{\pi(kb)^2 h(\lambda)}. \quad (26)$$

For a thin-walled Helmholtz resonator ($b = a$ in Figure 1) $h(\lambda)$ is given by [22, equation (3.7)]:

$$h(kb, k\ell) = 2 + \frac{4i}{\pi} \left(\gamma_e + \log \frac{k\ell}{4} \right) - \frac{1}{2} \sum_{m=-\infty}^{\infty} \frac{Q_m^2(kb)}{H'(kb)J'(kb)}, \quad (27)$$

where $Q_m(x) = J_m(x)H'_m(x) + J'_m(x)H_m(x)$ and γ_e is the Euler-Mascheroni constant. For the expression for $h(kb, ka, k\ell)$ for a thick-walled resonator ($a < b$) see [22, equation (3.7)], which we use to produce the results in Figure 6.

Performing the asymptotic expansion of $\epsilon = kb \ll 1$ in (27) we obtain

$$h(kb, k\ell) = 2 + \frac{4i}{\pi} \left(\gamma_e + \log \frac{k\ell}{4} \right) + \frac{2i}{\pi} \frac{1}{\epsilon^2} + \mathcal{O}\left(\frac{1}{\epsilon}\right), \quad (28)$$

where we do not expand the logarithmic term. From the above, and noting that $k\ell < kb$, we can conclude that $|h| \in \mathcal{O}(\epsilon^2)$ for frequencies away from resonance, which implies that $|z| \in \mathcal{O}(1)$. At resonance we have that $h(\lambda)$ is purely real, which occurs when $h(kb, k\ell) = 2$, and then $|z| \in \mathcal{O}(\epsilon^{-2})$. In other words, $z(\lambda)$ changes its order in ϵ when passing through resonance, which complicates an asymptotic analysis. Luckily, we do not need to perform an asymptotic expansion on $z(\lambda)$ to deduce simple effective formulae for the leading order term.

References

- [1] Giuseppe Failla, Alessandro Marzani, Antonio Palermo, Andrea Francesco Russillo, and Daniel Colquitt. Current developments in elastic and acoustic metamaterials science. *Philosophical Transactions of the Royal Society A: Mathematical, Physical and Engineering Sciences*, 382(2278):20230369, 2024.
- [2] R. A. Shelby, D. R. Smith, and S. Schultz. Experimental verification of a negative index of refraction. *Science*, 292(5514):77–79, 2001.
- [3] Biswajit Banerjee. *An introduction to metamaterials and waves in composites*. Taylor & Francis, 2011.
- [4] Steven A Cummer and David Schurig. One path to acoustic cloaking. *New Journal of Physics*, 9(3):45, mar 2007.
- [5] William J. Parnell and Tom Shearer. Antiplane elastic wave cloaking using metamaterials, homogenization and hyperelasticity. *Wave Motion*, 50(7):1140–1152, 2013. Advanced Modelling of Wave Propagation in Solids.
- [6] J. B. Pendry, D. Schurig, and D. R. Smith. Controlling electromagnetic fields. *Science*, 312(5781):1780–1782, 2006.
- [7] A.N. Norris and A.L. Shuvalov. Elastic cloaking theory. *Wave Motion*, 48(6):525–538, 2011. Special Issue on Cloaking of Wave Motion.
- [8] H. Nassar, B. Yousefzadeh, R. Fleury, M. Ruzzene, A. Alù, C. Daraio, A. N. Norris, G. Huang, and M. R. Haberman. Nonreciprocal acoustic and elastic materials. *Nature Reviews Materials*, 5:667–685, 2020.

- [9] A. J. Lawrence, Benjamin M. Goldsberry, Samuel P. Wallen, and Michael R. Haberman. Numerical study of acoustic focusing using a bianisotropic acoustic lens. *The Journal of the Acoustical Society of America*, 148(4):EL365–EL369, 10 2020.
- [10] Min Yang, Shuyu Chen, Caixing Fu, and Ping Sheng. Optimal sound-absorbing structures. *Mater. Horiz.*, 4:673–680, 2017.
- [11] S. Kumar, S. Tan, L. Zheng, and D. M. Kochmann. Inverse-designed spinodoid metamaterials. *Npj Computational Materials*, 6(1):1–10, 2020.
- [12] Simei Mao, Lirong Cheng, Houyu Chen, Xuanyi Liu, Zihan Geng, Qian Li, and Hongyan Fu. Multi-task topology optimization of photonic devices in low-dimensional fourier domain via deep learning. *Nanophotonics*, 12(5):1007–1018, 2023.
- [13] Meisam Askari et al. Additive manufacturing of metamaterials: A review. *Additive Manufacturing*, 36:101562, 2020.
- [14] Junxiang Fan, Lei Zhang, Shuaishuai Wei, Zhi Zhang, Seung-Kyum Choi, Bo Song, and Yusheng Shi. A review of additive manufacturing of metamaterials and developing trends. *Materials Today*, 50:303–328, 2021.
- [15] Anton Krynkin, Olga Umnova, Alvin Y B Chong, Shahram Taherzadeh, and Keith Attenborough. Scattering by coupled resonating elements in air. *Journal of Physics D: Applied Physics*, 44(12):125501, mar 2011.
- [16] Smith Michael J. A. and Abrahams I. David. Tailored acoustic metamaterials. part i. extremely thick-walled helmholtz resonator arrays. *Proc. R. Soc. A*, 478, 2022.
- [17] Smith Michael J. A. and Abrahams I. David. Tailored acoustic metamaterials. part ii. extremely thick-walled helmholtz resonator arrays. *Proc. R. Soc. A*, 478, 2022.
- [18] P. A. Martin, A. Maurel, and W. J. Parnell. Estimating the dynamic effective mass density of random composites. *The Journal of the Acoustical Society of America*, 128(2):571–577, 08 2010.
- [19] Artur L Gower and Gerhard Kristensson. Effective waves for random three-dimensional particulate materials. *New Journal of Physics*, 23(6):063083, 2021.
- [20] Artur L. Gower, Michael J. A. Smith, William J. Parnell, and I. David Abrahams. Reflection from a multi-species material and its transmitted effective wavenumber. *Proceedings of the Royal Society A: Mathematical, Physical and Engineering Sciences*, 474(2212):20170864, 2018.
- [21] Ping Sheng and Bart van Tiggelen. *Introduction to wave scattering, localization and mesoscopic phenomena*. Taylor & Francis, 2007.
- [22] Smith M. J. A., Cotterill P. A., Nigro D., Parnell W. J., and Abrahams I. D. Asymptotics of the meta-atom: plane wave scattering by a single helmholtz resonator. *Phil. Trans. R. Soc. A*, 380, 2022.
- [23] Tenneti C. Rao and Richard Barakat. Plane wave scattering from a cylindrical helmholtz resonator: Dirichlet case. *Optics Communications*, 164(4):223–232, 1999.
- [24] N.S. Bakhvalov and G.P. Panasenko. *Homogenisation: Averaging Processes in Periodic Media: Mathematical Problems in the Mechanics of Composite Materials*. Kluwer Academic Publishers, Dordrecht, 1989.
- [25] W.J. Parnell and I.D. Abrahams. Homogenization for wave propagation in periodic fibre-reinforced media with complex microstructure. i—theory. *Journal of the Mechanics and Physics of Solids*, 56(7):2521–2540, 2008.
- [26] Carlo Vanoni, Jaeuk Kim, Paul J. Steinhardt, and Salvatore Torquato. Dynamical properties of particulate composites derived from ultradense stealthy hyperuniform sphere packings, 2025.

- [27] Asma Sellami, Hervé Franklin, Anouar Njeh, and Pierre Maréchal. Effective bulk and mass densities of randomly distributed coated cylinders in fluid. *The Journal of the Acoustical Society of America*, 157(1):409–419, 01 2025.
- [28] Rachel Sun, Jet Lem, Yun Kai, Washington DeLima, and Carlos M. Portela. Tailored ultrasound propagation in microscale metamaterials via inertia design. *Science Advances*, 10(45):eadq6425, 2024.
- [29] Alexander Y. Piggott, Jesse Lu, Konstantinos G. Lagoudakis, Jan Petykiewicz, Thomas M. Babinec, and Jelena Vučković. Inverse design and demonstration of a compact and broadband on-chip wavelength demultiplexer. *Nature Photonics*, 9(6):374–377, 2015.
- [30] Leslie L. Foldy. The multiple scattering of waves. i. general theory of isotropic scattering by randomly distributed scatterers. *Phys. Rev.*, 67:107–119, feb 1945.
- [31] Aris Karnezis and Art L Gower. Calculating pair-correlations from random particle configurations. *arXiv preprint arXiv:2401.09236*, 2024.
- [32] Artur L Gower, Stuart C Hawkins, and Gerhard Kristensson. A model to validate effective waves in random particulate media: spherical symmetry. *Proceedings of the Royal Society A*, 479(2279):20230444, 2023.
- [33] K. K. Napal, P. S. Piva, and A. L. Gower. Effective t-matrix of a cylinder filled with a random two-dimensional particulate. *Proceedings of the Royal Society A: Mathematical, Physical and Engineering Sciences*, 480(2292):20230660, 2024.
- [34] P.C. Waterman. Matrix formulation of electromagnetic scattering. *Proceedings of the IEEE*, 53(8):805–812, 1965.
- [35] P. C. Waterman. Symmetry, unitarity, and geometry in electromagnetic scattering. *Phys. Rev. D*, 3:825–839, 1971.
- [36] Paul A. Martin. *Multiple Scattering: Interaction of Time-Harmonic Waves with N Obstacles*. Cambridge University Press, Cambridge, UK, 2006.
- [37] Artur L Gower and J Deakin. Multiplescattering.jl: A julia library for simulating, processing, and plotting multiple scattering of waves. version 0.1.21. *Github*, 2024.
- [38] Paulo S. Piva, Kevish K. Napal, and Art L. Gower. Acoustic waves in a halfspace material filled with random particulate, 2024.
- [39] Alexei T. Skvortsov, Ian R. MacGillivray, and Oleg A. Godin. Acoustic waves in a perforated cylinder. *The Journal of the Acoustical Society of America*, 157(3):1880–1888, 03 2025.